Brazilian Journal of Physics (2022) 52: 175
https://doi.org/10.1007/s13538-022-01179-4

GENERAL AND APPLIED PHYSICS

Production and Nondestructive Characterization of Shape Memory Alloys

Fadi Baghdadi[1] · **Aslihan Uzumcu**[1] · **Ilven Mutlu**[1]

Received: 25 October 2021 / Accepted: 2 August 2022 / Published online: 12 August 2022

Abstract
In this study, Ti–Ni-based and Fe-based shape memory alloys were fabricated by traditional powder metallurgy (press sinter). The green specimens were sintered, quenched, and precipitation hardened in a horizontal sliding flange tube furnace. This thermal process combines the sintering, quenching, and aging in a single step. Effects of the fabrication and heat treatment parameters on the mechanical properties were investigated. Elastic modulus of the alloys was characterized by destructive compression tests and non-destructive ultrasonic tests and eddy current tests. Nondestructive ultrasonic tests and eddy current tests were used in order to investigate the elastic modulus and microstructure. As the martensite and austenite phases have different elastic modulus values, martensite-austenite phase transformation temperature can be determined by ultrasonic velocity measurements and electrical conductivity measurements. Microstructure and corrosion properties were also investigated. Increasing Co and Sn content of the Ti–Ni alloy decreased the corrosion potential and increased the corrosion rate. Co and Sn additions to the Ti–Ni alloys enhanced the sinterability by liquid phase formation. Controlling the sintering and aging parameters was determined the mechanical properties. Elimination of the individual austenitizing, quenching, and aging steps can provide a cost advantage. Optimum aging temperatures were 400 °C for Ti–Ni-based alloys and 650 °C for Fe–Mn–Si-based alloys. The lowest transformation temperature values were in Ti–Ni–Co–Sn and Ti–Ni–Cr alloys, while the highest values were in Ti–Ni and Ti–Ni–Cu alloys. The lowest transformation temperature values were in Fe–Ni–Co–Sn and Fe–Mn–Si–Co alloys, while the highest values were in the Fe–Mn–Si alloy.

Keywords Shape memory · Ultrasonic test · Ti–Ni · Eddy current · Powder metallurgy

1 Introduction

Metallic shape memory alloys are unique class of alloys and are able to undergo very high reversible plastic deformation by using mechanical force or thermal cycles. Shape memory alloys can return to initially defined (undeformed) shape by heating (shape memory effect) or by removal of the stress (superelastic effect). This returning is due to the solid–solid, diffusionless, reversible, and displacive phase change. Shape memory alloys can exist in three structures (twinned martensite, detwinned martensite, and austenite). There are some requirements for the shape memory and superelasticity; martensitic transformations must be thermoelastic, there must be ordering in the microstructure, deformation mode must be twinning, and twinning and detwinning must be equal [1–7]. Shape memory materials have one-way shape memory effect and two-way shape memory effect. Shape recovery after heating is called thermal memory or one-way shape memory (OWSM). Recovery of the stress induced deformation can be described as superelasticity. In the OWSM, cooling from austenite temperatures does not cause a macroscopic shape change. Deformation is necessary in order to obtain the low-temperature shape. OWSM is an intrinsic property. In two-way effect (TWSM), the alloy remembers the both shapes. TWSM can be obtained by deformation, aging, and thermal cycling. TWSM effect is not an intrinsic property and needs a repeated thermomechanical treatment (training). Once the alloy has trained, it is possible to change the shape, between two shapes and without applied stress, only by changing the temperature [1–7].

There are commercially important Cu-based, Ni–Ti-based, and Fe-based SM alloys. Binary nickel–titanium

✉ Ilven Mutlu
imutlu@istanbul.edu.tr; imutlu@iuc.edu.tr

[1] Metallurgical and Materials Engineering Department, Istanbul University-Cerrahpasa, Istanbul, Turkey 34320

(Ni–Ti) alloys show excellent properties for biomedical applications such as corrosion resistance, biocompatible, non-magnetic properties, and responses at the temperature of the human body. Superelastic behavior, which fits stress–strain behavior of bone, makes it excellent material to stents. Hysteresis of SM alloys is ideal for stents. Bone exhibits recoverable strain, which is similar to NiTi. SM effect can be employed to activate the implants through body heat. Nitinol (Ni–Ti) is a very popular material in the several engineering applications. In general, Ni–Ti alloys show shape memory effect and superelasticity. Usually, nitinol includes Ni and Ti elements at equal atomic percentage. Shape memory effect is dependent on the composition and heat treatments. Precipitation at 300–500 °C causes migration of the Ni atoms to precipitate. This leads to increase in transformation temperatures. Above 500 °C, precipitates dissolve and Ni atoms diffuse back, and transformation temperatures decrease. To achieve balance between driving force and diffusion, maximum precipitation rate occurs at 400 °C. At high temperatures, there is work hardening, solid-solution strengthening, aging, grain refinement, strengthening TiNi by increasing the critical shear stress [8–10]. Binary Ti–Ni alloys have transformation temperatures below 100 °C. Transformation temperatures decrease with increasing Ni content. Precipitates decrease the Ni content of the matrix. Point defects can affet the transformation. Point defercts can be varied by alloying or heat treatments. Intermediate rhombohedral R-phase (pre-martensite) can be obtained in the microstructure, with increasing Ni content, aging, alloying, and thermal cycling. B2-R transformation is attractive because of the small hysteresis behavior [5–10].

The shape memory behavior of the Fe-based alloys is lower than NiTi-based shape memory alloys or Cu-based shape memory alloys. But, Fe-based shape memory alloys are cheaper than Cu-based and NiTi-based alloys. There are two types of Fe-based shape memory alloys; Fe–Ni–Co-based shape memory alloys and Fe–Mn–Si-based shape memory alloys. Fe-based alloys (Fe–Mn–Si and Fe–Ni–Co–Ti) are attractive due to their cold workability and lower cost. But Fe alloys exhibit lower superelasticity since they show dislocation-triggered slip and tend to form irreversible martensite. So, matrix needs to be strengthened. Fe–Ni–Co–Al–Ta/Nb–B alloys exhibit a potential, but their superelasticity is poor. Although Fe–Mn–Si alloys, using γ (face centered cubic, fcc) to ε (hexagonal-close packed, hcp) transformation, have been used, Fe–Ni–Co alloys, using γ (face centered cubic, fcc) to α (body-centered tetragonal, bct) transformation, have not yet been applied. Fe–Ni–Co alloys are a precipitation-type shape memory alloy. Martensitic transformation hysteresis can be decreased by increasing the hardness, improving the martensite tetragonality, reducing the transformation temperature. These properties can be adjusted by precipitates. Martensite exhibits lath martensite, butterfly martensite, A-type martensite, lenticular martensite, and thin plate martensite. Only thin plate morphology facilitates the formation of thermoelastic transformation. Superelasticity can be obtained in Fe–Ni–Co–Al/Ti alloys by thermoelastic martensitic transformation by precipitates. Ni decreases the Ms temperature and stabilizes the austenite. Ni is essential for precipitation of fcc phases (Ni_3Al/Ni_3Ti). Co addition improves the hardness, favors the thin plate type martensite, and decreases the change of volume. Al or Ti is used to form Ni_3Ti/Ni_3Al phases. Ta or Nb are γ phase (Ni_3Ti or Ni_3Al)-stabilizing elements, leading to thermoelastic transformation and increased strength (hardness). Fe–Ni–Co–Ti/Al are brittle because of precipitates of Ni_3Ti/Ni_3Al. But, precipitates of NiTi/NiAl can enhance the ductility. By aging at 600 °C the γ precipitates can be obtained. Non-aged samples did not show non-thermoelastic transformation. Alloying additions to the Fe–Mn–Si alloys enhance the mechanical properties. These alloys have higher hysteresis. In the Fe–Mn–Si alloys, there are different martensitic transformations such as face-centered cubic (FCC) to body-centered cubic (BCC) or body-centered tetragonal (BCT), face-centered cubic (FCC) to face-centered tertagonal (FCT), or face-centered cubic (FCC) to hexagonal-close packed (HCP). In the Fe–Mn–Si-based alloys, high temperature austenite phase transforms to martensite at room temperature. Stress-induced martensitic transformation in the Fe–Mn–Si alloys occurs by creation of stacking faults. As in the Fe–Mn–Si-based alloys, there is a FCC to HCP transformation; in the Fe–Ni-based shape memory alloys, there is FCC to BCT phase transformation. Although Fe–Mn–Si-based shape memory alloys are used in industrial applications, Fe–Ni–Co alloys are not used yet. In the Fe–Ni–Co alloys, shape memory effect is small due to non-thermoelastic transformation [11–20].

The aim of this study is the production of the Ti–Ni-based (Ti–Ni–Co, Ti–Ni–Sn, Ti–Ni–Co–Sn), Fe-based (Fe–Ni–Co–Ti, Fe–Ni–Co–Sn, and Fe–Mn–Si–Sn) shape memory alloy specimens for implant applications. The specimens were produced by traditional powder metallurgy, which is a solid-state process. The samples were sintered, quenched, and aged in a horizontal sliding flange tube furnace. This thermal process combines the sintering, quenching, and aging in a single step. Aging heat treatment for adjustment of shape memory behavior was considered. Effects of the process parameters on the mechanical properties were investigated. Elastic modulus of the specimens was characterized by destructive compression tests and nondestructive ultrasonic tests. Nondestructive ultrasonic test was used to investigate the elastic modulus and microstructure. Martensite-austenite phase transformation temperature was investigated by using ultrasonic measurements. In general, ultrasonic velocity is related to elastic modulus and

density of the materials. The traditional casting-based metal production and forming processes are not suitable to obtain homogenaeous chemical compositions of Ti–Ni alloys because of the segregation due to the density differences of the alloying elements. Segregation in the solid-state powder metallurgy-based alloys is small.

2 Experimental

2.1 Green Specimen Production

In this study, Ti–Ni based (Ti–Ni–Co, Ti–Ni–Sn, Ti–Ni–Co–Sn), and Fe-based (Fe–Ni–Co, Fe–Ni–Co–Sn, and Fe–Mn–Si–Sn)-based shape memory alloy specimens were fabricated by solid-state based traditional powder metallurgy (press-sinter) route [21–23]. Chemical compositions of the alloys were (45–49)Ti–(50)Ni–(1–5)Co, (45–49)Ti–(50)Ni–(1–5)Sn, (47)Ti–(50)Ni–(1)Co–(2)Sn, (87–89)Fe–(5)Ni–(5)Co–(1–3)Sn, and (65–69)Fe–(25)Mn–(5)Si–(1–5)Sn. First, powder mixtures were ball milled (mechanical alloying) with ZrO_2 balls (3 mm) with a rotational speed of 400 rpm for about 6 h. Six hours of mechanical alloying time was sufficient for homogenization to be used in production of these alloys. Metal powder to ball ratio was 1/10. In addition, mechanical alloying can produce grain refinement, which also effects the microstructure and mechanical properties. Polyvinylalcohol (PVA) was used as a binder for green strength before sintering (Merck, Germany). After mechanical alloying, PVA solution (6 wt. %) was added to the metal powder. PVA solution was consisted of 3 wt. % PVA and distilled water. Metal powder was mixed manually with the PVA solution. Powder-binder mixtures were compacted at 300 MPa. Height of the cylindrical samples was about 18–20 mm and the diameter of the samples was 12 mm.

2.2 Heat Treatment

Single step sintering-aging heat treatment was carried out within a horizontal sliding flange tube furnace. Figure 1 shows the sliding flange horizontal tube furnace and schematic sintering-aging heat treatment procedure. The sintering process was consisted of heating at a ramp rate of 6 °C/min to 390 °C with a dwell time of 30 min (thermal debinding), followed by heating at rate of 10 °C/min to the sintering temperatures. Thermal debinding temperature of the PVA was determined to be ~ 390 °C by using thermo

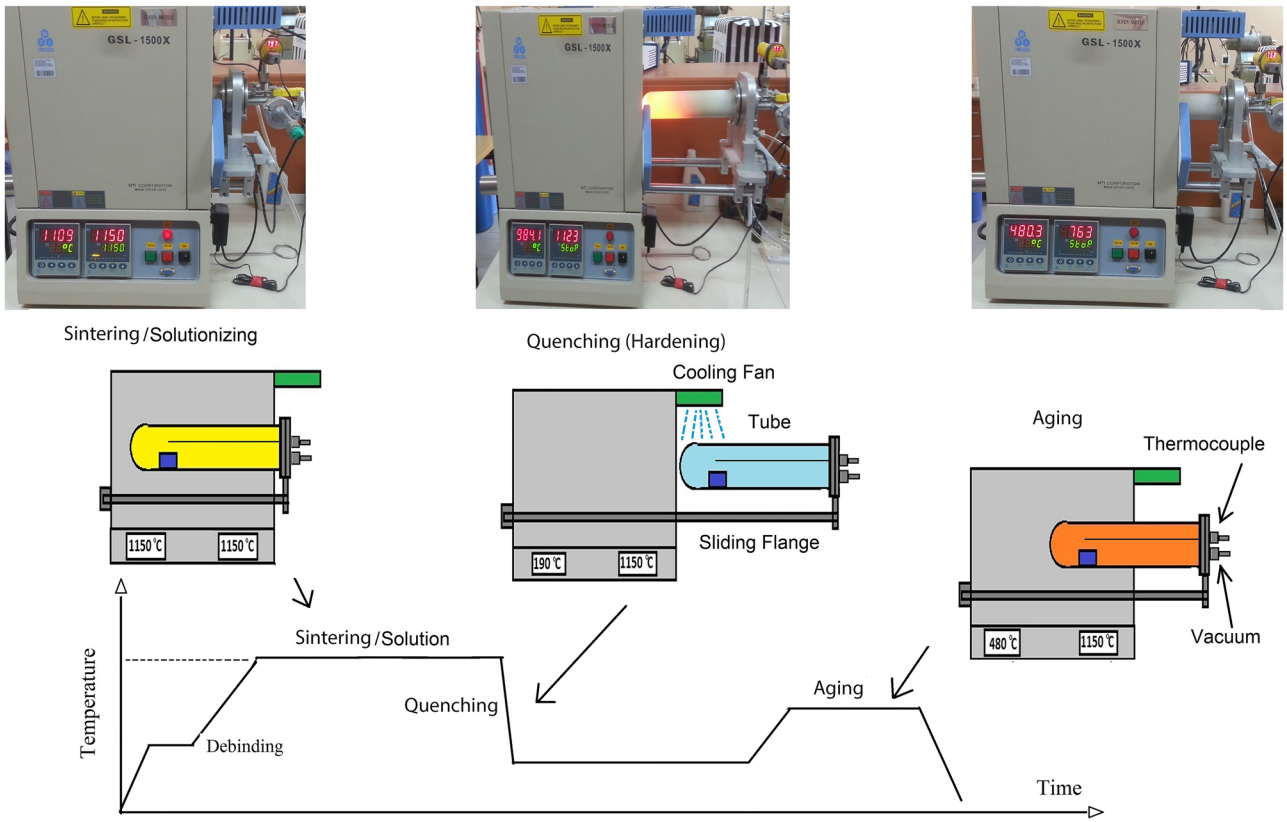

Fig. 1 Sliding flange tube furnace and schematic sintering-aging heat treatment procedure

gravimetric analysis (TA, SDT Q600). The PVA in the green specimens was thermally removed as part of sintering cycle. The green specimens were sintered at 1100–1200 °C temperatures for 60 min. The sintering of Ti–Ni-based and Fe alloy–based specimens was performed in vacuum in a horizontal tube furnace (MTI, USA). As the Ti–Ni alloys are very sensitive even to very small amounts of atmospheric impurities, vacuum furnace was employed for sintering of the Ti–Ni-based alloys. Then, the tube was removed out from the heating zone of the furnace and samples were rapidly cooled directly from the sintering temperature at the cooling rate of 1.0–3.0 °C/s. A cooling fan was employed at the end tip of the heating tube of the furnace to increase the post-sintering cooling rate. Subsequently, the specimens were precipitation hardened. Ti–Ni-based specimens were aged for 60 min at 350–450 °C, while the Fe-based alloys were aged at 500–700 °C.

2.3 Characterisation of Microstructure and Mechanical Properties

A microstructural characterization analysis of the specimens was performed by scanning electron microscope (FEI, FEG 450). Mechanical properties of the samples were studied by the compression test performed on a material testing machine (Devotrans, Turkey). In the present study, the martensite-austenite phase transformation temperatures of the shape memory Fe-based alloys and Ti–Ni-based alloys were determined by ultrasonic velocity measurements. As martensite and austenite phases have different elastic modulus values, martensite-austenite phase transformation temperature can be determined by ultrasonic velocity measurements. In general, ultrasonic velocity is related to elastic modulus and density of the material. Ultrasonic wave is influenced by the microstructure (phases). It is advantageous to use nondestructive ultrasonic test since the destructive method is time consuming and requires destruction (compression or tension). Nondestructive ultrasonic method can be employed for detection of defects and to investigate mechanical properties and microstructure. In the present study, the elastic modulus was also determined by using a pulse-receiver-type ultrasonic instrument (General Electric, USA). Elastic modulus was calculated by the following well-known Eq. (1) [25]. V_T and V_L are transverse and longitudinal velocities and ρ is density. Four-megahertz normal beam longitudinal wave transducer was employed for the ultrasonic velocity measurements [24, 25].

$$E = \rho V_T^2 \frac{3V_L^2 - 4V_T^2}{V_L^2 - V_T^2} \quad (1)$$

Electrical conductivity of the alloys was investigated by using WeldCheck, EThER NDE eddy current device. Electrical conductivity was determined according to international annealed copper standard (IACS). The electrical conductivity of the annealed copper was defined to be 100% IACS at 20 °C, and conductivity of the specimen was determined with respect to % IACS. Before the electrical conductivity test, the eddy current device was calibrated by using dual conductivity reference standard with known conductivity in % IACS. The electrical conductivity is a useful property since values are affected by chemical composition and microstructure. Conductivity measurements can be used for investigating the heat treatments.

2.4 Electrochemical Corrosion Tests

Electrochemical corrosion experiments were done using a potentiostat (Interface 1000, Gamry). Evaluation of the tests was carried out by using softwares (Framework, Gamry). Initially, open-circuit potential (OCP) was conducted for about 7200 s. Tafel and linear polarization resistance tests were employed in order to determine the corrosion rate values.

3 Results and Discussion

In the present study, shape memory Ti–Ni-based (Ti–Ni, Ti–Ni–Co, Ti–Ni–Sn, Ti–Ni–Co–Sn) specimens were fabricated by powder metallurgy method by using irregular-shaped fine metal powders. Figure 2 given below exhibits the SEM pictures of the irregular shaped fine (a) Ni, (b) Ti, (c) Co, and (d) Sn powders.

Shape memory Fe–Mn–Si-based and Fe–Ni–Co-based alloy specimens were also fabricated by powder metallurgy method by using fine metal powders. Figure 3 given below exhibits the SEM pictures of the (a) Fe, (b) Mn, (c) Si, and (d) Sn powders.

Figure 4 given below shows the SEM picture of the microstructure of the sintered shape memory 45Ti–45Ni–5Co–5Sn alloy specimen. As seen from the figure, there is a suitable sintering between the metal powder particles. In addition, there are no microcracks or macrocracks in the microstructure of the sintered alloys. As shown in Fig. 4, the microstructure of the 45Ti–45Ni–5Co–5Sn alloy specimen consists of alpha (α) parent phase (matrix), some precipitates (intermetalics) along the grain boundaries, and some retained austenite phase.

Figure 5 given below shows the SEM picture of the microstructure of the sintered shape memory Fe–Mn–Si alloy. As seen from Fig. 5, there is a suitable sintering between the metal powder particles. In addition, there are no microcracks or macrocracks in the microstructure of the sintered alloys. As shown in Fig. 5, the microstructure of the Fe–Mn–Si alloy specimen consists of ε (hexagonal-close

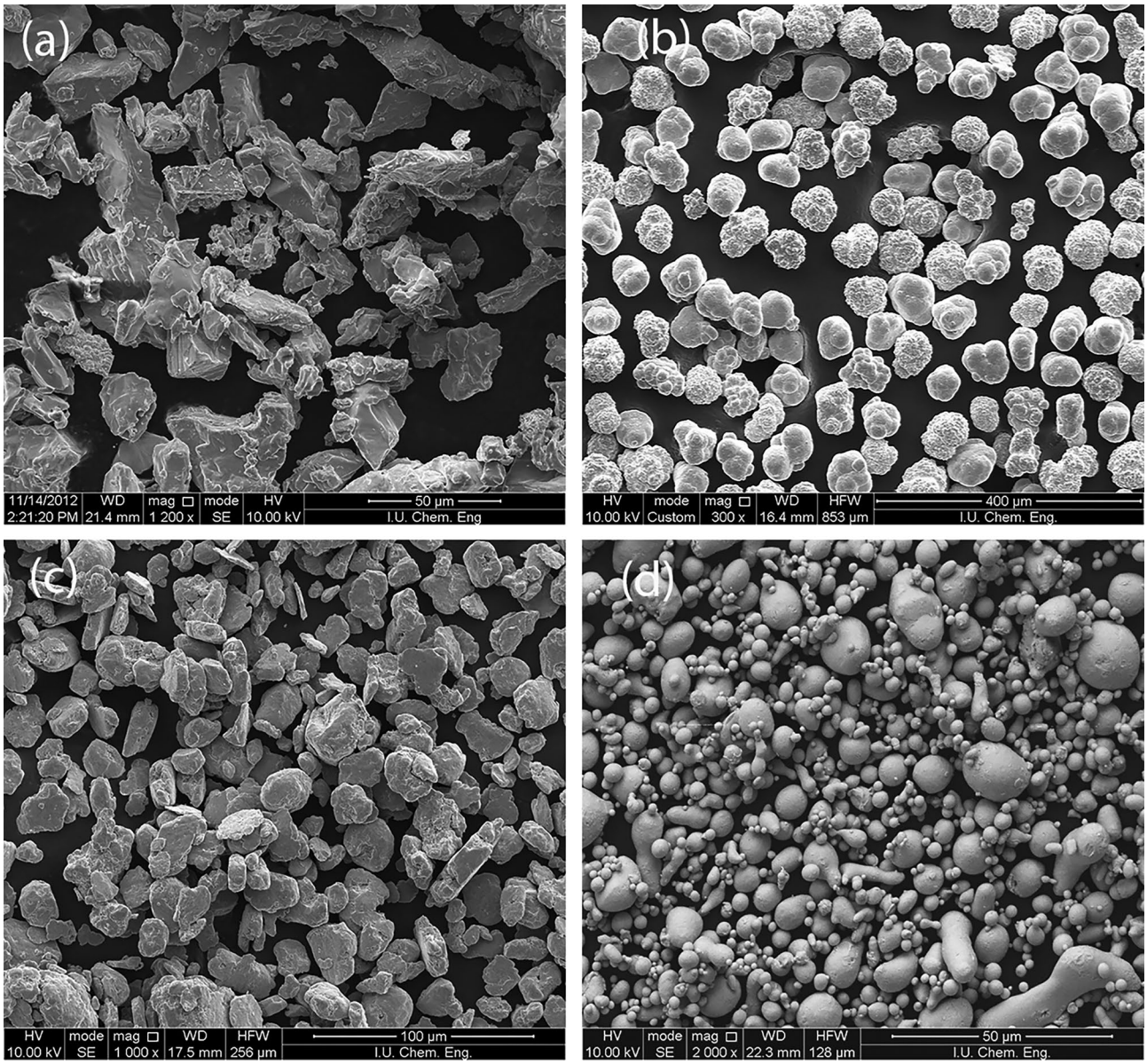

Fig. 2 SEM picture of **a** Ti, **b** Ni, **c** Co, and **d** Sn powders

packed) martensite phase and some retained γ (face centered cubic) austenite phase and some δ-ferrite phase. Also, some α^1-martensite phase can be seen due to low Mn content of the alloy. In general, Mn additions higher than 21% stabilize the ε-martensite with respect to α′-martensite. Moreover, Mn stabilizes the γ-austenite phase.

Figure 6 shows the effect of aging temperature on the electrical conductivity (IACS %) of (a) Ti–Ni alloy specimen and (b) Fe–Mn–Si alloy specimen. Shape memory effect is dependent on the chemical composition and heat treatments (phases). Variation of Ni content shifts the transformation temperatures. Precipitations during aging cause migration of Ni atoms to participates, which leads to increase in transformation temperatures. At high temperatures, precipitates dissolve and Ni atoms diffuse back. This causes the transformation temperature decrease. To achieve balance between driving force and diffusion, maximum precipitation rate occurs at 400 °C, which is the best temperature for aging. Increase in transformation temperatures comes from thermally induced stresses and defects. At high temperatures, there is energy for diffusion; but it is difficult for same atoms to form precipitates as temperature increases. Small-amount Co and Sn additions to the binary Ti–Ni shape memory alloys decrease the transformation temperature and separates the B2/R and R/B19′ transitions. In the aging, boundaries of Ti_3Ni_4 precipitates are coherent, and lattices

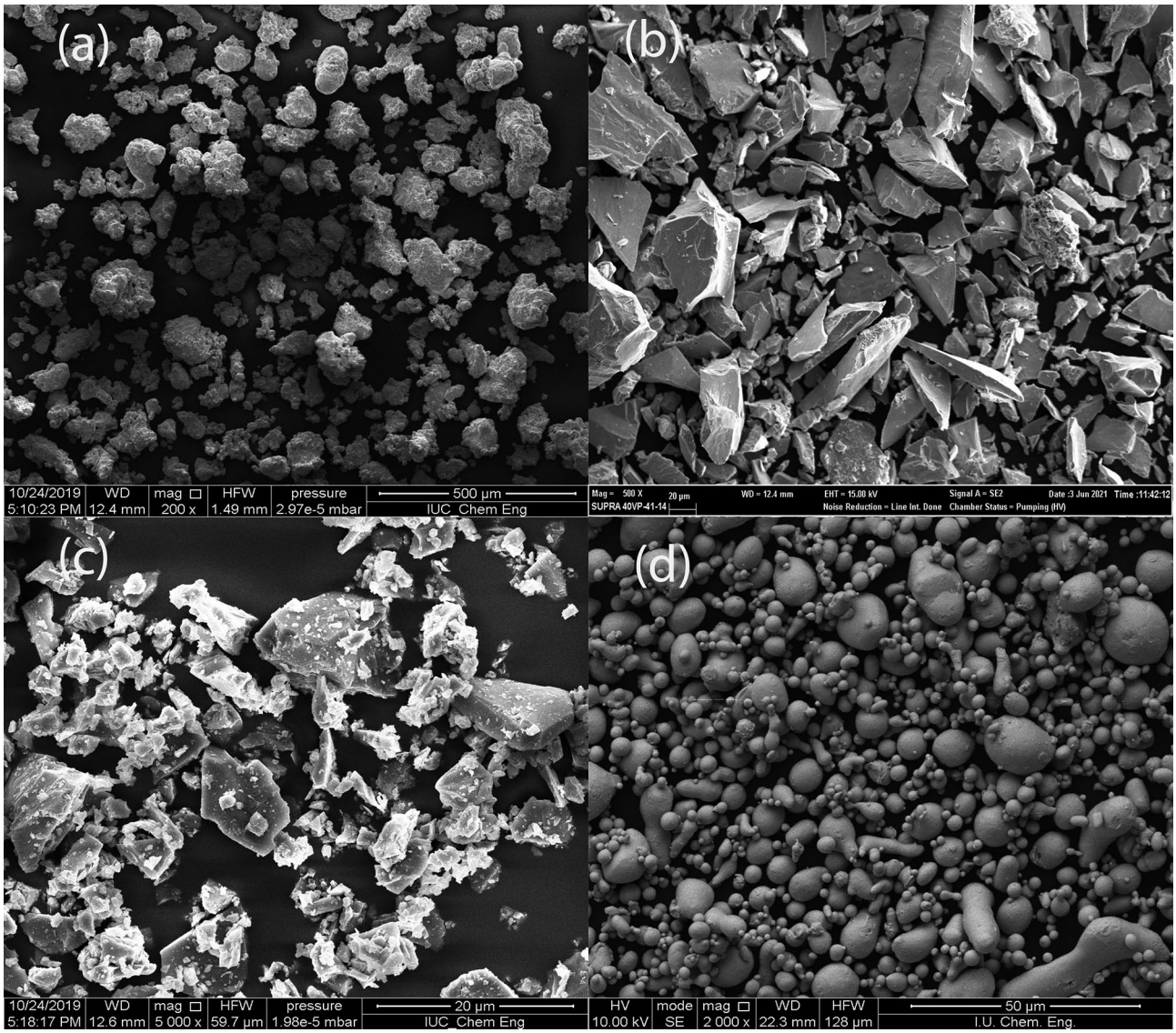

Fig. 3 SEM picture of **a** Fe, **b** Mn, **c** Si, and **d** Sn powder

are distorted by the coherent stress field. As the aging time increases, the precipitates grow and lose their coherency [8–10]. As shown in Fig. 6, electrical conductivity of the specimens was changed with the aging parameters. In general, electrical conductivity values of different phases are different. Phases and precipitates in the microstructure of the specimens were changed with the aging temperature. Electrical conductivity values are affected by chemical composition and microstructure (phases and precipitates). Conductivity measurements can be used in order to investigate the microstructure. Electrical conductivity of materials depends on electronic mobility, crystal structure, and defects, such as interstitials, dislocations, and grain boundaries. The reasons of the increase in the electrical conductivity with increasing aging temperature are purification of matrix by segregation of solute atoms and formation of semi-coherent phases, and vacancy diffusion mechanism which removes the vacancies (scattering centers). Depending on the increase in precipitation rate, foreign atoms, which act as scattering centers, segregate from the matrix. Equilibrium precipitates are larger particles and increase in size as the aging proceeds, thus minimizing scattering effect. Conductivity becomes lower when concentration of the solute atoms in the solid solution increases, while becomes higher when alloying elements are precipitated. The conductivity is influenced by amount of alloying elements in the solid solution and nature of precipitates.

Figure 7 given below shows the effect of aging temperature on the elastic modulus of the sintered shape memory Ti–Ni–Co and Fe–Mn–Si alloy specimens. As shown in

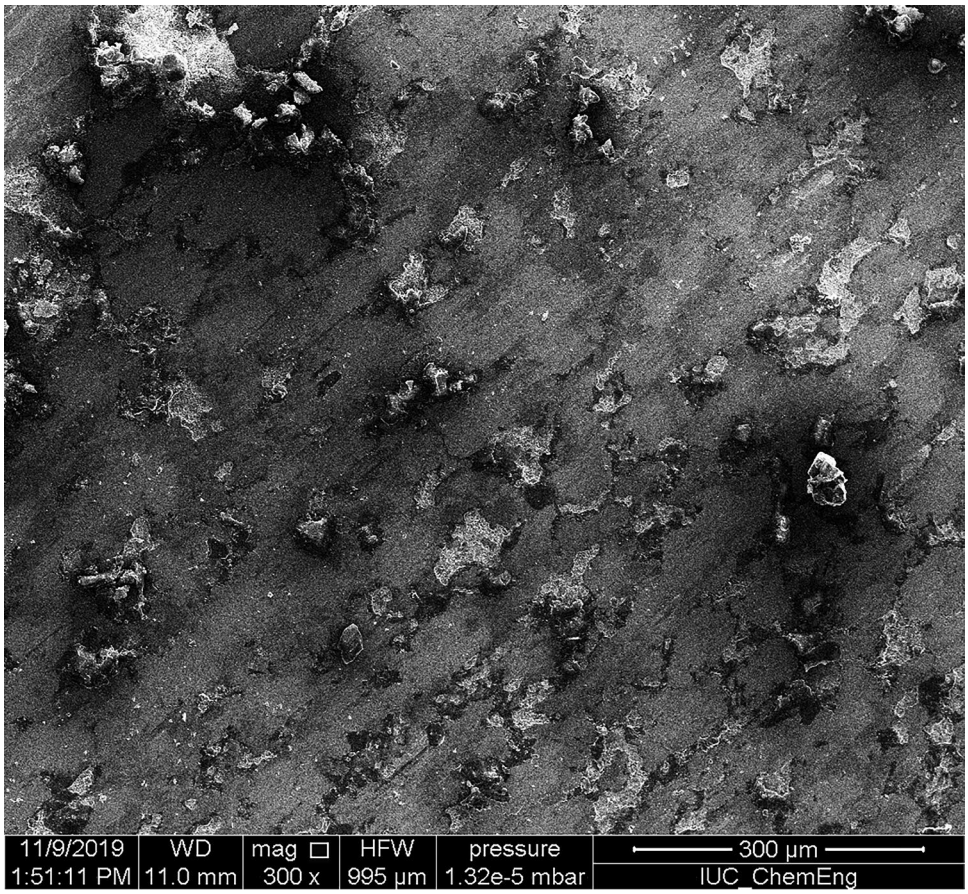

Fig. 4 SEM picture of the sintered Ti–Ni–Co–Sn alloy

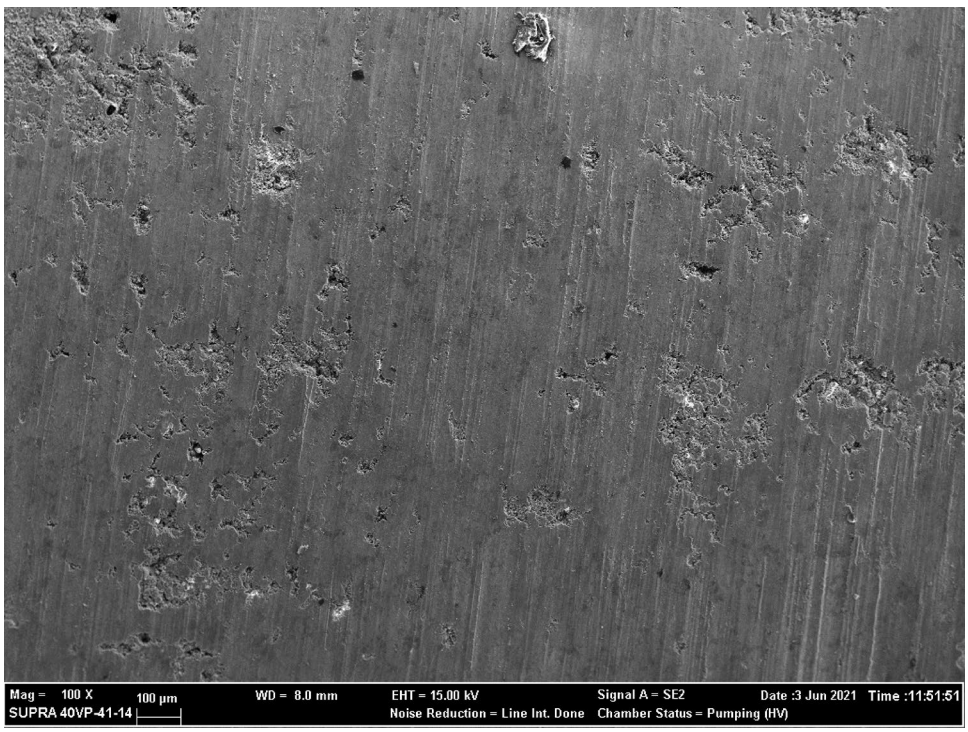

Fig. 5 SEM picture of the sintered Fe–Mn–Si alloy

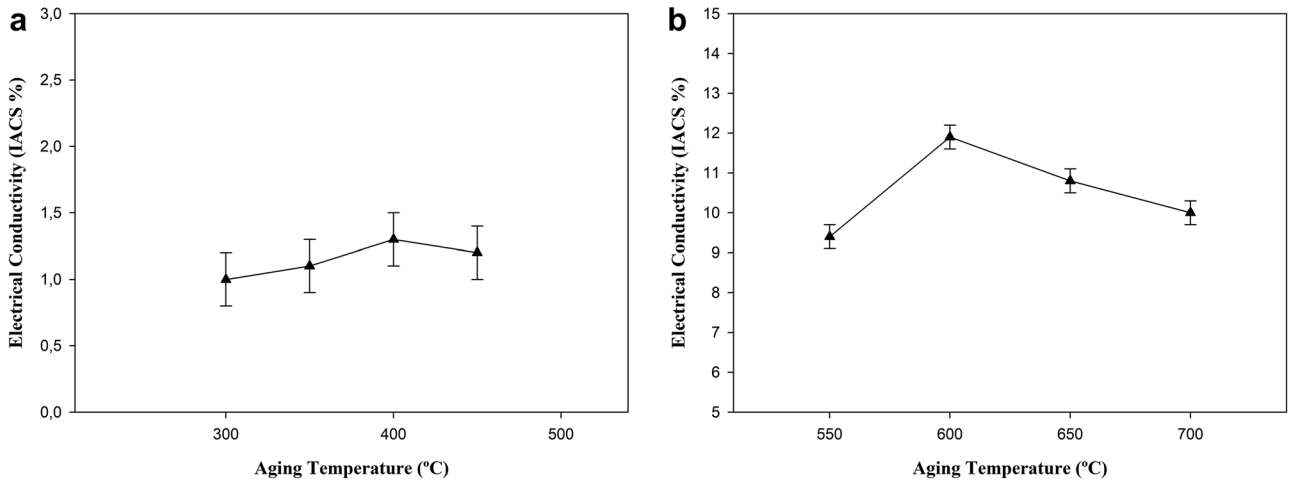

Fig. 6 Effect of aging temperature on the electrical conductivity of the **a** Ti–Ni specimen and **b** Fe–Mn–Si specimen

Fig. 7, optimum aging temperatures were about 400 °C for Ti–Ni-based alloys and 650 °C for Fe–Mn–Si-based alloys. Elastic modulus was slightly decreased after 400 °C for Ti–Ni and decreased after 650 °C for Fe–Mn–Si alloys due to overaging. As shown in Fig. 7, Young's modulus changes with heat treatment temperature. Young's modulus, which represents the binding force between atoms, is one of the material characteristics and relates to crystal structure, alloying, and phase transformation. Young's modulus of a multiphase alloy is determined by the elastic modulus and the volume fractions of its constituent phases. Aging promotes precipitation of new phases from the solution-treated alloy and results in variation of aged microstructures including the phase composition and amount of each phase at different aging temperatures, which is responsible for variation of Young's modulus. The Young's modulus of an alloy is sensitive to phases precipitated at different aging temperatures, and the alternation in microstructures is the reason which results in changes in Young's modulus.

The martensite-austenite phase transformation temperatures of the shape memory Fe-based alloys and Ti–Ni-based alloys were determined by ultrasonic velocity measurements. As martensite and austenite phases have different elastic modulus values, martensite-austenite phase transformation temperature can be determined by ultrasonic velocity measurements. Ultrasonic velocity is related to elastic modulus and density of the material. Ultrasonic wave is influenced by the microstructure (phases). Elastic modulus was determined by using a pulse-receiver-type ultrasonic instrument. It is advantageous to use nondestructive ultrasonic test since the destructive method is time consuming and requires destruction. Figure 8 illustrates the effect of temperature on the elastic modulus of the sintered shape memory (a) Ti–Ni-based

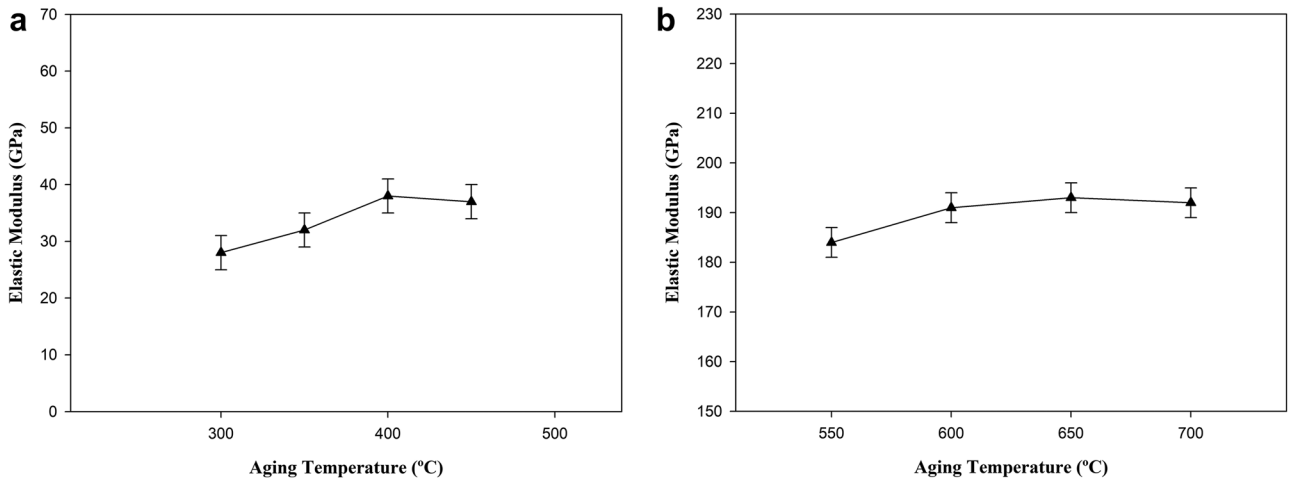

Fig. 7 Effect of aging temperature on elastic modulus of **a** Ti–Ni specimen and **b** Fe–Mn–Si specimen

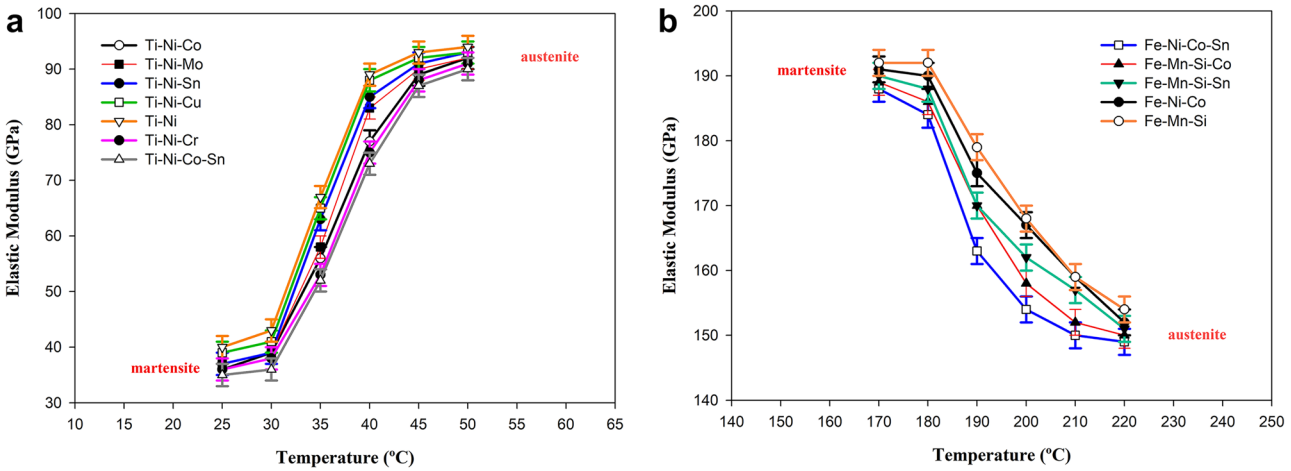

Fig. 8 Effect of temperature on the elastic modulus of the **a** Ti–Ni based alloys and **b** Fe-based alloys

alloys and (b) Fe-based alloys. Elastic modulus values were calculated by using ultrasonic velocity measurements. As seen from Fig. 8a, austenite–martensite phase transformation temperatures of the sintered shape memory Ti–Ni-based alloys were about 30–40 °C. As the martensite and austenite phases have different elastic modulus values from each other, austenite–martensite phase transformation temperature can be determined by the ultrasonic velocity measurements. Figure 8b shows the effect of temperature on the elastic modulus of the sintered Fe-based alloys. Transformation temperatures of the sintered shape memory Fe-based alloys were about 180–200 °C. As the martensite and austenite phases have different elastic modulus values from each other, martensite-austenite phase transformation temperature of the alloy can be determined by the velocity measurements. As shown in Fig. 8, ultrasonic velocity in the specimens is related to Young's modulus. Ultrasonic velocity in solids is related to elastic modulus of the material, which can change with aging because of change in matrix composition and precipitation of different phases. The increase in the ultrasonic velocity with aging was attributed to the increased volume fraction of precipitates, which was contributed to the increased elastic modulus. Ultrasonic velocity increases as a result of reduction of distortions of lattice due to the breakdown of supersaturated solid solution. Initial increase in the ultrasonic velocity during precipitation is attributed to the increased volume fraction of precipitates, which increases the elastic modulus. However, in overaged condition, the loss of coherency strain leads to decrease in the elastic modulus of the interface and reduces the ultrasonic velocity.

Figure 9 illustrates the effect of temperature on the electrical conductivity (IACS %) of the sintered shape memory (a) Ti–Ni-based alloys and (b) Fe-based alloys. Electrical conductivity of the metals and alloys depends on the

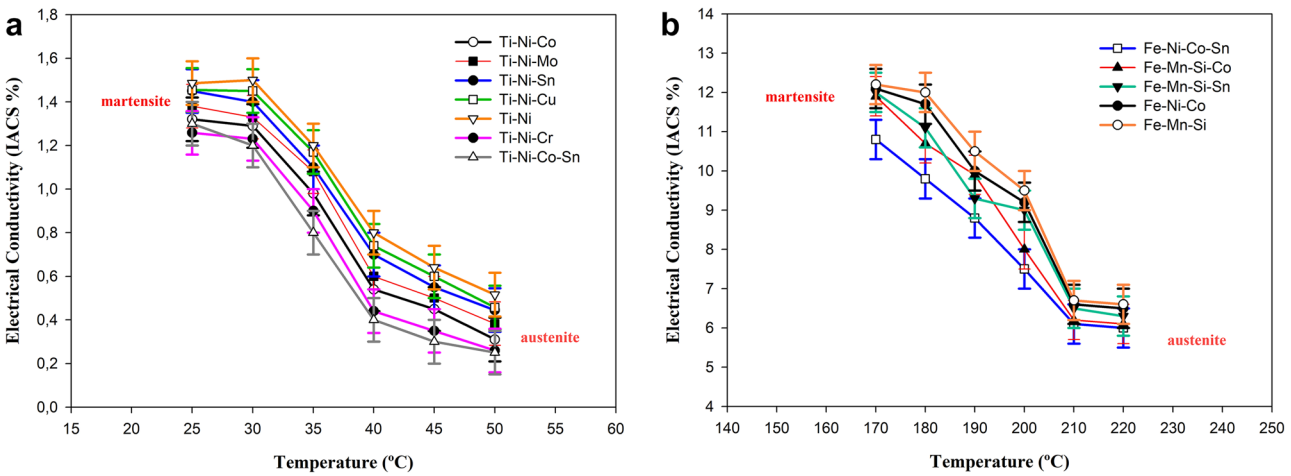

Fig. 9 Effect of temperature on the electrical conductivity of the **a** Ti–Ni based alloys and **b** Fe-based alloys

electronic mobility, microstructure, and imperfections in the lattice. Electrical conductivity determination by using eddy current test can be employed for the determination of the microstructural phases of metals. As seen from Fig. 9, electrical conductivity values of the alloys were decreased with increasing temperature. Nondestructive ultrasonic and eddy current methods can be used for characterization of the microstructure and the transformation temperature. Elastic modulus of the Fe-based and Ti–Ni-based alloys was determined by using ultrasonic measurements. As shown in Fig. 9, electrical conductivity values of different phases are different. Phases and precipitates in the microstructure of the specimens were changed with temperature. Electrical conductivity values are affected by microstructure (phases).

The martensite-austenite phase transformation temperatures of the shape memory Fe-based alloys and Ti–Ni-based alloys were determined by nondestructive ultrasonic velocity measurements. As martensite and austenite phases have different elastic modulus values, martensite-austenite transformation temperature can be determined by ultrasonic velocity measurements. In general, ultrasonic velocity is related to elastic modulus and density of the material. Ultrasonic wave is influenced by the microstructure (phases). Figure 10 shows the martensite-austenite phase transformation temperatures of the shape memory Ti–Ni-based alloys. Transformation temperatures were changed with the alloying elements. The lowest transformation temperature values were in Ti–Ni–Co–Sn and Ti–Ni–Cr alloys. The highest transformation temperature values were observed in the Ti–Ni and Ti–Ni–Cu alloys. As shown in Fig. 10, alloying elements decreased the martensite-austenite phase transformation temperature of the Ti–Ni alloys. Alloying elements changed the Ni content of the matrix and diffusion rate of the Ni, which was attributed to the change in the transformation temperature.

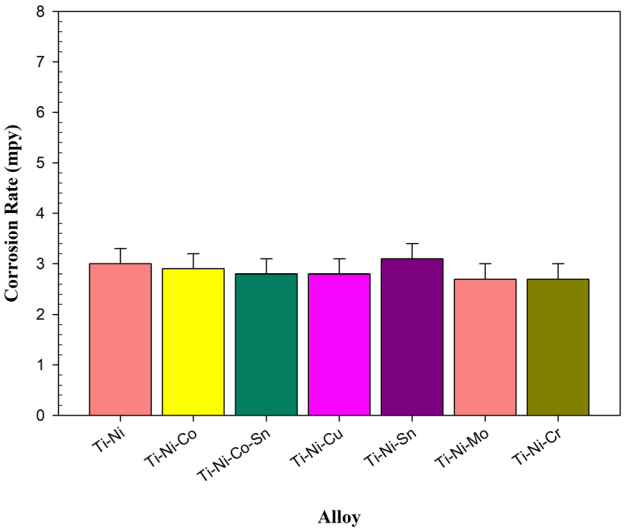

Fig. 11 Electrochemical corrosion rate values of the TiNi-based alloys

Figure 11 shows the electrochemical corrosion rates of the shape memory Ti–Ni-based alloys. Electrochemical corrosion rates were changed with the alloying elements. The lowest corrosion rate values were in Ti–Ni–Cr and Ti–Ni–Mo alloys. The highest corrosion rate was observed in the Ti–Ni–Sn alloy. As shown in Fig. 11, Sn addition increased the corrosion rate of the Ti–Ni alloys, which was attributed to the lower standard electrode potential of the Sn. Also, Sn produced phases which produce galvanic corrosion and increase corrosion rate. On the other hand, Co, Cu, Mo, and Cr additions decreased the corrosion rate of the Ti–Ni alloys.

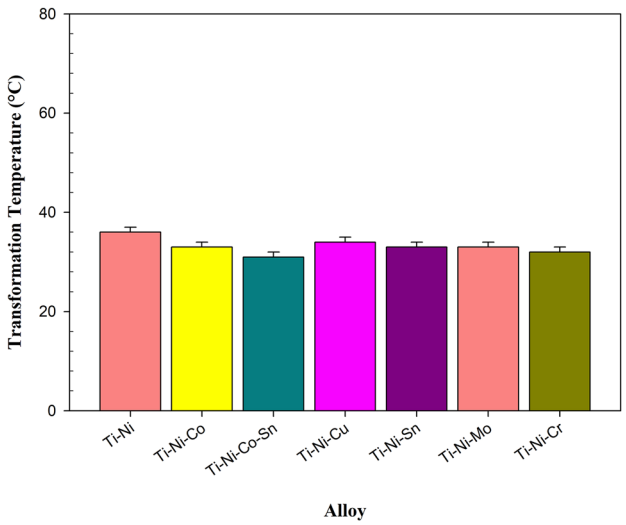

Fig. 10 Transformation temperature values of the TiNi-based alloys

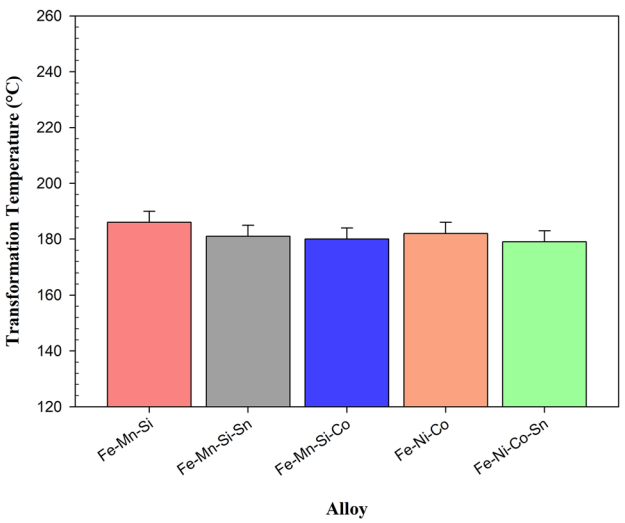

Fig. 12 Transformation temperature values of the Fe-based alloys

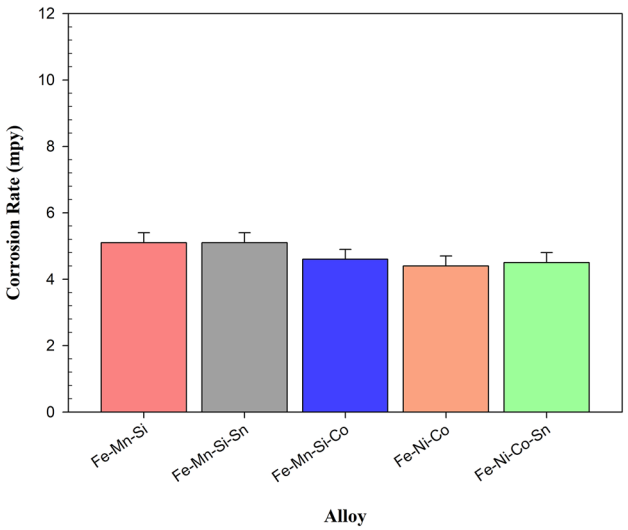

Fig. 13 Electrochemical corrosion rates of the Fe-based alloys

Figure 12 shows the martensite-austenite phase transformation temperatures of the shape memory Fe-based alloys. Transformation temperatures were changed with the alloying elements. The lowest transformation temperature values were in Fe–Ni–Co–Sn and Fe–Mn–Si–Co alloys. The highest transformation temperature values were observed in the Fe–Mn–Si alloy. As shown in Fig. 12, alloying elements decreased the martensite-austenite phase transformation temperature of the Fe–Ni–Co-based and Fe–Mn–Si-based alloys.

Figure 13 shows the electrochemical corrosion rates of the shape memory Fe-based alloys. Electrochemical corrosion rates were changed with the alloying elements. The lowest corrosion rate value was in Fe–Ni–Co alloy. The highest corrosion rates were observed in the Fe–Mn–Si–Sn and Fe–Mn–Si alloys. As shown in Fig. 13, Sn addition slightly increased the corrosion rate of the alloy, which was attributed to the lower standard electrode potential of the Sn. Also, Sn produced phases which produce galvanic corrosion and increase corrosion rate. On the other hand, Co addition slightly decreased the corrosion rate.

4 Conclusions

In this study, Ti–Ni-based and Fe–Mn–Si-based shape memory alloy specimens were fabricated by powder metallurgy method. The specimens were sintered, quenched, and precipitation hardened in a horizontal sliding flange tube furnace. This thermal process combines the sintering, quenching, and aging heat treatments in a single step. Effects of heat treatment process parameters on the mechanical properties were investigated. Elastic modulus of the specimens was characterized by destructive compression tests and non-destructive ultrasonic tests. Nondestructive ultrasonic test was employed to investigate the elastic modulus and microstructure. Martensite-austenite phase transformation temperature was investigated by using ultrasonic velocity measurements. The martensite-austenite phase transformation temperatures of the shape memory Fe-based alloys and Ti–Ni-based alloys were determined by ultrasonic velocity measurements. As martensite and austenite phases have different elastic modulus values, martensite-austenite phase transformation temperature can be determined by ultrasonic measurements. Ultrasonic velocity is related to elastic modulus and density of the material. Ultrasonic wave is influenced by the microstructure. In the present study, elastic modulus was determined by using a pulse-receiver-type ultrasonic instrument. It is advantageous to use nondestructive ultrasonic test since the destructive method is time consuming and requires destruction. Microstructure and electrochemical corrosion properties of the alloys were also investigated. Casting-based production and forming process are not suitable to obtain a homogenaeous material. Chemical composition of cast Ti-Ni alloys is not uniform due to density differences of the alloying elements. Segregation in the solid-state based powder metallurgy alloys is lower than the cast alloys. Effects of the sintering-aging process parameters on the mechanical properties of the specimens were investigated. Increasing Co and Sn content of the Ti–Ni alloy decreased the corrosion potential and increased the electrochemical corrosion current density. Co and Sn additions to the Ti–Ni alloys enhanced the sinterability of the alloy by liquid phase formation. Controlling the sintering and aging parameters was determined the mechanical properties of the samples. Elimination of the individual austenitizing, quenching, and aging steps can provide a cost advantage. Optimum aging (precipitation hardening) temperatures were about 400 °C for Ti–Ni-based alloys and 650 °C for Fe–Mn–Si-based alloys. The lowest transformation temperature values were in Ti–Ni–Co–Sn and Ti–Ni–Cr alloys. The highest transformation temperature values were observed in the Ti–Ni and Ti–Ni–Cu alloys. The lowest transformation temperature values were in Fe–Ni–Co–Sn and Fe–Mn–Si–Co alloys. The highest transformation temperature values were observed in the Fe–Mn–Si alloy.

Funding This work was supported partially by Scientific Research Projects Coordination Unit of Istanbul University-Cerrahpasa, Project Numbers of 35176, 35631, and 34045.

Declarations

Conflict of Interest The authors declare no competing interests.

References

1. M.H. Elahinia, M. Hashemi, M. Tabesh, S.B. Bhaduri, Prog. Mater Sci. **57**, 911–946 (2012)
2. J.M. Jani, M. Leary, A. Subic, M.A. Gibson, Mater. Des. **56**, 1078–1113 (2014)
3. L. Sun, W.M. Huang, Z. Ding, Y. Zhao, C.C. Wangb, H. Purnawali, C. Tang, Mater. Des. **33**, 577–640 (2012)
4. R. DesRoches, J. McCormick, M. Delemont. J. Struct. Eng. **130**(1), 38–46 (2004)
5. J. Kim, Y. Im, J. Noh, S. Miyazaki, T. Nam, Scripta Mater. **65**, 608–610 (2011)
6. L.M. Isola, B.F. Malvasio, M.F. Giordana, J. Malarria, J. Alloy. Compd. **818**, 152904 (2020)
7. C. Cisse, W. Zaki, T.B. Zineb, Int. J. Plast **76**, 244–284 (2016)
8. R.I. Babicheva, K.Y. Mulyukov, Appl. Phys. A **116**, 1857–1865 (2014)
9. S.H. Chang, K.H. Lin. S.K. Wu, Materials **10**, 704 (2017)
10. J. Ma, I. Karaman, R.D. Noebe, Int. Mater. Rev. **55**(5), 257–315 (2010)
11. B. Liu, Y.F. Zheng, L. Ruan, Mater. Lett. **65**, 540–543 (2011)
12. D. Lee, T. Omori, K. Han, Y. Hayakawa, R. Kainuma, Shap. Mem. Superelasticity **4**, 102–111 (2018)
13. M. Jin, Y. Geng, S. Zuo, X. Jin, Materials Today: Proceedings **2S**, S837–S840 (2015)
14. T. Omori, S. Abe, Y. Tanaka, D.Y. Lee, K. Ishida, R. Kainuma, Scripta Mater. **69**, 812–815 (2013)
15. C.H. Yang, H.C. Lin, K.M. Lin, Mater. Sci. Eng., A **518**, 139–143 (2009)
16. H.R. Koohdar, M. Nili-Ahmadabadi, M. Habibi-Parsa, H.R. Jafarian, H. Ghasemi-Nanesa, H. Shirazi, Mater. Sci. Eng., A **658**, 86–90 (2016)
17. S.H. Adarsh, V. Sampa, Mater. Res. Express **6**, 075701 (2019)
18. Y. Tanaka, R. Kainuma, T. Omori, K. Ishida, Materials Today: Proceedings **2S**, S485–S492 (2015)
19. Z. Chen, W. Peng. Funct Mater Lett. **13**(1), 1950096 (2020)
20. X. Ren, R. Das, P. Tran, T.G. Ngo, Y.M. Xie, Smart Mater. Struct. **27**, 114–173 (2018)
21. R.M. German, *Powder Metallurgy Science*, Metal Powder Industries Federation, Princeton, New Jersey. (1994)
22. G.S. Upadhyaya, Powder Metallurgy, Cambridge International Science Publishing, England. 1 898326 40 1 (2002)
23. ASM Handbook, Volume 7, Powder Metal Technologies and Applications, ASM International, USA, 0–87170–387–4. (1998)
24. I. Mutlu, S. Ekinci, E. Oktay, J. Mater. Eng. Perform. **238**(6), 2083–2091 (2014)
25. C. Hellier, *Handbook of Nondestructive Evaluation* (McGraw-Hill, New York, 2003)